

A Dual-Gate Altermagnetic Tunnel Junction Based on Bilayer Cr₂SeO

Yunfei Gao^a, Aolin Li^{a,*}, Zesen Fu^a, Bei Zhang^a, Haiming Duan^a, Fangping Ouyang^{a, b,*}

^a School of Physics and Technology, Xinjiang Key Laboratory of Solid State Physics and Devices, Xinjiang University, Urumqi 830046, People's Republic of China

^b School of Physics, Institute of Quantum Physics, Hunan Key Laboratory for Super-Microstructure and Ultrafast Process, and Hunan Key Laboratory of Nanophononics and Devices, Central South University, Changsha 410083, People's Republic of China

^c State Key Laboratory of Powder Metallurgy, and Powder Metallurgy Research Institute, Central South University, Changsha 410083, People's Republic of China

* Corresponding author E-mail: liaolin628@xju.edu.cn (A. Li); ouyangfp06@tsinghua.org.cn (F. Ouyang)

Altermagnets demonstrate significant potential in spintronics due to their unique non-relativistic spin-splitting properties, yet altermagnetic devices still face challenges in efficiently switching logic states. Here, we report electrostatically controllable spin-momentum locking in bilayer Cr₂SeO and design a dual-gate altermagnetic tunnel junction (AMTJ), which can switch between high and low resistance states without switching the Néel vector. First-principles calculations demonstrate that vertical electric field can induce significant spin splitting in bilayer Cr₂SeO. Reversing the electric field direction can alter the spin-momentum locking in bilayer Cr₂SeO. Leveraging this electric-field-tunable spin splitting, the dual-gate AMTJ exhibits an ultrahigh tunneling magnetoresistance (TMR) ratio of 10⁷. This work provides theoretical support for the design of fully electrically controlled AMTJs and demonstrates their great potential for applications in spintronic devices.

I. INTRODUCTION

Altermagnets, an emergent class of magnetic materials, have sparked extensive interest in both fundamental research and application design. Unlike conventional ferromagnets and antiferromagnets, altermagnets exhibit zero net magnetization while demonstrating significant non-relativistic momentum-dependent spin-splitting, making them a special class of collinear antiferromagnets.[1-4] Researchers have identified multiple altermagnetic materials, including MnTe, CrSb, Fe₂Se₂O, Ca(CoN)₂, V₂SSeO and so on.[5-11] Altermagnetism can be induced in two-dimensional (2D) antiferromagnetic bilayers through twisting.[3,12] Due to unique spin-momentum locking of altermagnets, they have rapidly become a research focus in spintronics.[7,8,13-18]

Magnetic tunnel junction (MTJ) plays a pivotal role in spintronic applications.[19-28] MTJ is generally a sandwich structure composed of ferromagnet/tunneling barrier/ferromagnet. By applying external magnetic fields, the magnetization directions of the two ferromagnetic electrodes in MTJs can be switched

between parallel configuration (PC) and antiparallel configuration (APC), thereby modulating the devices between high resistance and low resistance states. However, MTJs are susceptible to interferences from stray fields in ferromagnetic materials and external magnetic fields. This susceptibility affects their stability and high-density integration at the nanoscale. The Néel vector in altermagnets effectively resists interference from stray fields and external magnetic fields, which contributes to the high-density integration of MTJs. Some researchers have designed altermagnetic tunnel junctions (AMTJs) based on altermagnetic materials, realizing the application of altermagnetic materials in the field of spintronics.[13,14]

Most studies on AMTJs rely on the reversal of the Néel vector to achieve the switching between high and low resistance states. Switching the Néel vector relies on current drive.[29,30] Besides switching the Néel vector, AMTJs can also be realized by applying gate voltages, which offers lower power consumption. Recent research has found that bilayer Cr₂SO can achieve spin-valley locking through the application of an electric field.[31] Electric field control of such bilayer system achieves the same effect as switching the Néel vector in monolayer altermagnet.

In this work, density functional theory (DFT) calculations indicate that applying an electric field can lift the band degeneracy in bilayer Cr₂SeO, enabling spin-valley locking. For valleys located at the same high-symmetry point, their spin polarization directions are identical. The spin polarization directions of valleys are opposite at different high-symmetry points. The reversal of the electric field direction leads to a corresponding flip in the spin polarization direction of the X and Y valleys. As the electric field strength increases, the band gap of bilayer Cr₂SeO decreases. When the electric field strength reaches ± 0.85 V/Å, bilayer Cr₂SeO undergoes a semiconductor-to-metal phase transition. Based on the aforementioned mechanism, we design a dual-gate AMTJ, which is fully electrically controlled and does not change the Néel vector of left and right electrodes. The crux of implementing such the AMTJ lies in applying independently tunable gate voltages with controllable strength and direction to two electrode regions. We apply gate voltages sufficient to induce the metallic phase in both the left and right electrodes. The AMTJ manifests a low resistance state when the dual-gate voltages are configured such that the spin directions of the conductive channels at the Fermi level in both left and right electrodes are parallel near the high-symmetry points X and Y; conversely, the AMTJ enters a high resistance state when the spin directions are antiparallel. Non-equilibrium Green's function formalism combined with DFT (NEGF-DFT) calculations reveal that under finite bias voltages, the AMTJ exhibits ultrahigh tunneling magnetoresistance (TMR), reaching magnitudes of up to 10^7 .

II. CALCULATION METHOD

The structural optimization and electronic structure calculations are carried out using the Vienna ab initio simulation package (VASP) based on DFT,[32] where the exchange-correlation interaction is treated with the generalized gradient approximation (GGA) of the Perdew-Burke-Ernzerhof (PBE) form. The projector

augmented wave (PAW) pseudopotentials are employed and the energy cutoff is set to 500 eV.[33,34] A Γ -centered $17 \times 17 \times 1$ k-point mesh is used for Brillouin zone integration. The force criterion for structural optimization and the energy criterion are set to be 0.01 eV/Å and 10^{-6} eV, respectively. To properly deal with the strong correlation effect in Cr atoms, the DFT + U method is adopted with an effective Coulomb parameter $U = 3.55$ eV for 3d orbital.[1] A vacuum layer thicker than 15 Å is applied to avoid interactions between periodic images and the van der Waals interactions are considered using the DFT-D3 method of Grimme.[35]

The electronic transport properties of the device are calculated using Nanodcal package based on the NEGF-DFT method,[36] where the exchange-correlation interaction is described by the GGA of the PBE form. The double-zeta polarized (DZP) basis is employed with the energy cutoff of 100 Hartree, and the energy convergence criterion is set to 10^{-5} eV for the transport calculations. The k-point mesh of the electrodes is set to $1 \times 17 \times 100$. The spin-dependent transmission T_σ as a function of energy E and bias V can be described by the following equation:

$$T_\sigma(E, V) = \text{Tr}[\Gamma_L(E, V)G^R(E, V)\Gamma_R(E, V)G^A(E, V)], \quad (1)$$

where σ represents spin direction (\uparrow, \downarrow), $\Gamma_{L/R}$ is the linewidth function, which describes the coupling between the left or right electrodes and the central region. G^R and G^A are the retarded and advanced Green's functions, respectively. I_σ is defined by the following Landauer-Büttiker formula:

$$I_\sigma(V) = \frac{e}{h} \int_{\mu_L}^{\mu_R} T_\sigma(E, V) [f(E - \mu_L) - f(E - \mu_R)] dE, \quad (2)$$

where h is Plank's constant, e is the electron charge, $\mu_{L/R} = E_F \pm \frac{eV}{2}$ are the chemical potentials with bias V , and $f(E - \mu_{L/R})$ are the Fermi-Dirac distribution functions of electrons in the two electrodes under non-equilibrium conditions.

III. RESULTS AND DISCUSSIONS

Monolayer Cr₂SeO emerges as a canonical 2D altermagnet, as shown in Fig. 1(a). After structural optimization, monolayer Cr₂SeO exhibits a lattice parameter of 3.72 Å. The high-symmetry points of the Brillouin zone are indicated in Fig. 1(a). Monolayer Cr₂SeO exhibits a bandgap of 0.59 eV and non-relativistic momentum-dependent spin splitting, as shown in Fig. 1(c). Distinct spin-polarized valleys emerge near the high-symmetry points X and Y, where VBM and CBM show opposite spin directions. Switching the Néel vector can flip the spin polarization directions of the bands. We construct bilayer Cr₂SeO via van der Waals stacking and show the lowest-energy magnetic configuration of bilayer Cr₂SeO, as shown in Fig. 1(b). The band structure shown in Fig. 1(d) indicates bilayer Cr₂SeO preserves its semiconducting character with spin-degenerate bands and a bandgap of 0.59 eV.

To modulate the band structure of bilayer Cr_2SeO , we apply a vertical electric field. Computational results demonstrate that when the electric field is applied, the potential difference between the upper and lower layers breaks the system's symmetry, breaking the spin degeneracy and inducing significant spin splitting at the high-symmetry points X and Y, while reducing the bandgap. When a positive electric field is applied, the valleys at the high-symmetry point X exhibit spin-up polarization, while those at the high-symmetry point Y show spin-down polarization. Conversely, when a negative electric field is applied, the spin polarizations at X and Y valleys reverse. When the electric field strength reaches $\pm 0.85 \text{ V}/\text{\AA}$, the bands at the high-symmetry points X and Y cross the Fermi level, and the bilayer Cr_2SeO undergoes a semiconductor-to-metal phase transition, as shown in Figs. 2(a) and 2(b).

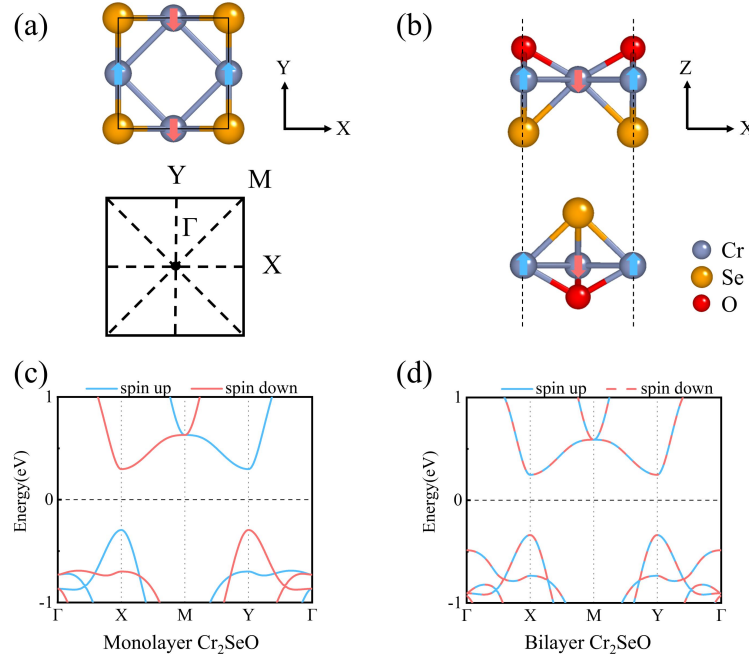


FIG. 1. (a) Top view and high-symmetry points in the first Brillouin zone of monolayer Cr_2SeO . (b) Side view of bilayer Cr_2SeO . Red and blue arrows indicate the different magnetic moment directions. Band structures of (c) monolayer Cr_2SeO and (d) bilayer Cr_2SeO .

The electric field dependence of the bandgap at the X and Y valleys is presented in Fig. 2(c). As shown in Figs. 2(a) and 2(b), the spin directions of bands near the high-symmetry points X and Y at the Fermi level in bilayer Cr_2SeO are controlled by the direction of the electric field. This property provides a key mechanism for electrically controlled AMTJs.

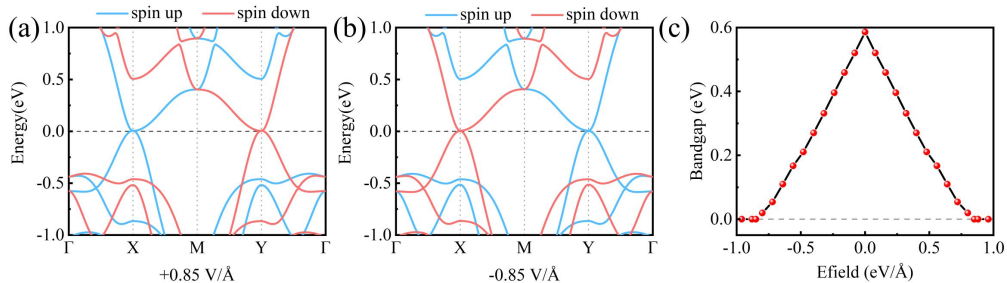


FIG. 2. Band structures of bilayer Cr_2SeO under applied vertical electric fields of (a) $+ 0.85 \text{ V}/\text{\AA}$ and (b) $- 0.85$

V/Å. (c) Electric field dependence of the bandgap in bilayer Cr_2SeO .

Based on the aforementioned electric field control mechanism, we design an electrically controlled bilayer Cr_2SeO AMTJ, as shown in Fig. 3(a). This AMTJ only consists of bilayer Cr_2SeO , and we apply two gates to the electrode regions and buffer layers. The left electrode and its buffer layer are subjected to a fixed-direction gate voltage, while the right electrode and its buffer layer can be applied with either parallel or antiparallel gate voltage relative to the left electrode. When the gate voltages of the left and right electrodes are the same, the AMTJ enters the PC state. When the gate voltages in the left and right electrodes are oppositely oriented, the AMTJ enters the APC state. When the AMTJ is in the PC state, it exhibits low resistance; when in the APC state, it exhibits high resistance.

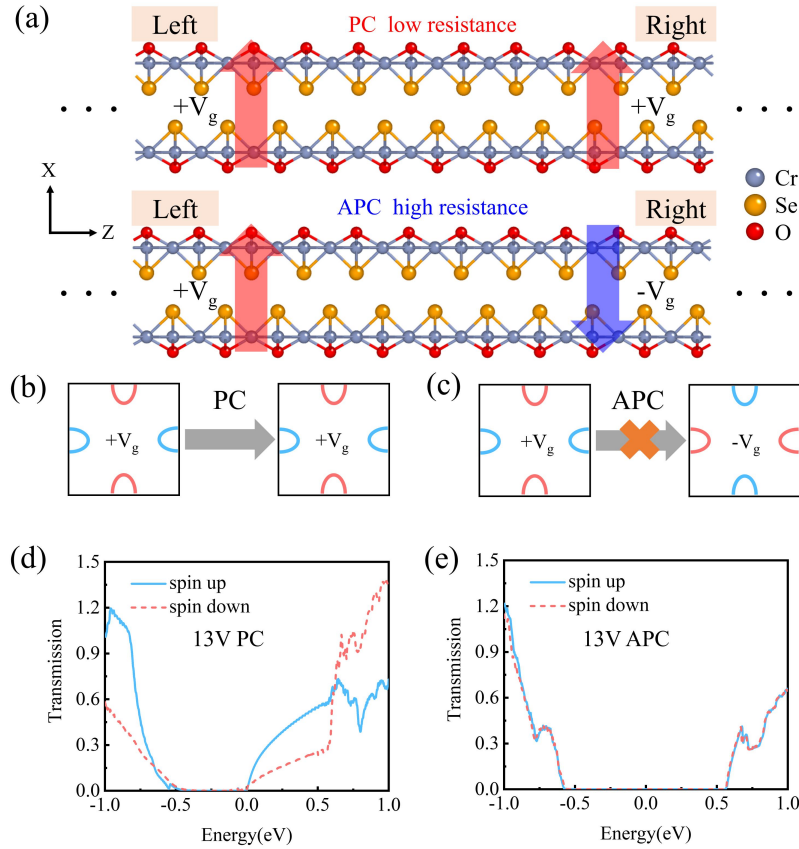


FIG. 3. (a) Schematic diagram of the bilayer Cr_2SeO AMTJ, with electrodes and buffer layers under two gates. The qualitative 2D Fermi surfaces of the left and right electrodes of the bilayer Cr_2SeO AMTJ in the (b) PC and (c) APC states. Red and blue respectively represent different spin directions. The similarities and differences in the spin directions of conductive channels enable the current to be switched on and off. The electron transmission spectra of the bilayer Cr_2SeO AMTJ at $V_{\text{gate}} = 13$ V without bias voltage in the (d) PC and (e) APC states, respectively.

As shown in Figs. 3(b) and 3(c), we use the qualitative 2D Fermi surfaces to illustrate the operational principle of bilayer Cr_2SeO AMTJ. In the PC state, the states with the same \mathbf{k} vector in the left and right electrodes at the Fermi level are spin-matched, respectively allowing spin-up and spin-down electrons to transfer near the high-symmetry points. Due to quantum tunneling effects, both spin-up and spin-down electrons can transmit through the AMTJ, resulting in the low resistance

state. Conversely, in the APC state, the states with the same \mathbf{k} vector in the left and right electrodes at the Fermi level are spin-mismatched. Due to the tunneling barrier and the spin mismatch for the states with the same \mathbf{k} vector, the transport of both spin-up and spin-down electrons is significantly suppressed, resulting in the high resistance state. Thus, by switching the gate voltage directions, the matching and mismatching of spin states between the left and right electrodes of the bilayer Cr_2SeO AMTJ can be easily controlled, enabling efficient switching between low and high resistance states.

To verify the feasibility of the bilayer Cr_2SeO AMTJ, we employ the NEGF-DFT method to calculate the electronic transport properties of the AMTJ. Figs. 3(d) and 3(e) present the equilibrium-state (without bias voltage) electron transmission spectra for the PC and APC states at $V_{\text{gate}} = 13$ V, respectively. In the PC state, the transmission spectrum shows that both spin-up and spin-down electrons have transmission coefficients at the Fermi level, indicating that both spin-up and spin-down electrons can be transported throughout the device when a finite bias is applied. In the APC state, transmission spectrum exhibits vanishing transmission coefficients for all electrons near the Fermi level, corresponding to the high resistance state of the AMTJ.

To investigate the performance of the bilayer Cr_2SeO AMTJ, we calculate the variation of TMR with gate voltages under zero bias voltage, as shown in Fig. 4(a). The TMR is defined as $\text{TMR} = (G_{\text{PC}} - G_{\text{APC}})/G_{\text{APC}}$, where G_{PC} and G_{APC} denote the total conductance in the PC and APC states, respectively. The TMR reaches a maximum of 8.65×10^5 at $V_{\text{gate}} = 13$ V. When $V_{\text{gate}} = 17$ V, the AMTJ still has a TMR value of 3.58×10^4 . To further study the device performance under non-equilibrium states, we calculate its TMR under finite bias voltage at $V_{\text{gate}} = 13$ V, the TMR is defined as $\text{TMR} = (I_{\text{PC}} - I_{\text{APC}})/I_{\text{APC}}$, where I_{PC} and I_{APC} denote the total currents in the PC and APC states, respectively. When $V_{\text{gate}} = 13$ V, the AMTJ maintains ultrahigh TMR on the order of 10^5 within a bias voltage range from -0.08 V to 0.08 V, with a maximum TMR value of 6.06×10^7 . These results demonstrate that the bilayer Cr_2SeO AMTJ exhibits a giant magnetoresistance effect that significantly outperforms both most of novel 2D MTJs and conventional 3D MTJs,[14,21,28,37-39] making it a highly promising candidate for next-generation spintronic devices.

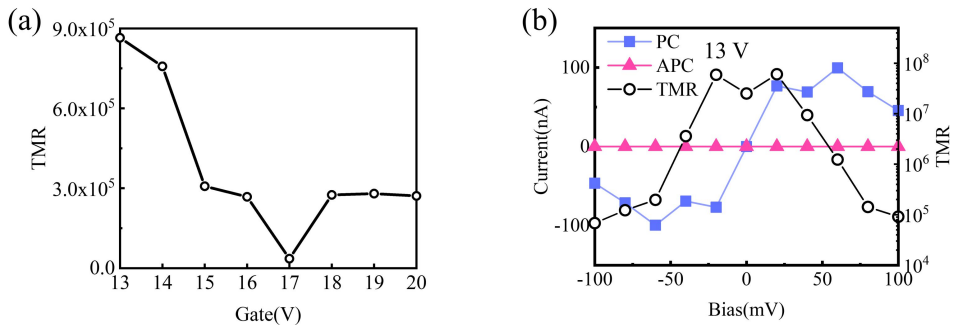


FIG. 4. (a) The variation of TMR in the bilayer Cr_2SeO AMTJ with gate voltages under zero bias voltage. The PC state and APC state currents, as well as the TMR, in the bilayer Cr_2SeO AMTJ at $V_{\text{gate}} = 13$ V under finite bias voltages. When the bias voltage is zero, the TMR is calculated using the transmission coefficient instead of the current.

IV. CONCLUSION

In summary, vertical electric field infliction is a potentially effective strategised for breaking the spin degeneracy in the X and Y valleys of bilayer Cr₂SeO, giving rise to spin-polarized valleys. For valleys located at the same high-symmetry point, their spin polarization directions are identical. The spin polarization directions of valleys are opposite at different high-symmetry points. The spin polarization directions are determined by the direction of the applied electric field. When the electric field strength is sufficiently high, bilayer Cr₂SeO undergoes a semiconductor-to-metal phase transition. Based on these findings, we design a dual-gate bilayer Cr₂SeO AMTJ without changing the Néel vector. The AMTJ exhibits ultrahigh tunneling magnetoresistance (TMR), reaching magnitudes of up to 10⁷. More importantly, this work has broad implications. The proposed approach can be employed to design AMTJs by all bilayer systems with similar band characteristics and magnetic ground states. Our work not only overcomes the limitation of conventional MTJs that rely on magnetic field manipulation but also provides a promising approach for designing atomically thin AMTJs with ultrahigh TMR.

Acknowledgements

This work was funded by the Key Project of the Natural Science Program of Xinjiang Uygur Autonomous Region (Grant No. 2023D01D03), the XJU Innovation Project for Ph.D candidate (XJU2024BS049), the Tianchi-Talent Project for Young Doctors of Xinjiang Uygur Autonomous Region, the National Natural Science Foundation of China (Grant Nos.52073308; 12564028), the Tianshan Innovation Team Program of Xinjiang Uygur Autonomous Region (Grant No. 2023D14001), and the State Key Laboratory of Powder Metallurgy at Central South University. We gratefully acknowledge HZWTECH for providing computation facilities. This work was carried out in part using computing resources at the High-Performance Computing Center of Central South University.

Declaration of competing interest

The authors declare no competing financial interest.

Data availability

Data will be made available on request.

References

- [1] S.-D. Guo, X.-S. Guo, K. Cheng, K. Wang, and Y. S. Ang, *Appl. Phys. Lett.* **123**, 082401 (2023).
- [2] W. Sun, W. Wang, C. Yang, R. Hu, S. Yan, S. Huang, and Z. Cheng, *Nano Lett.* **24**, 11179 (2024).
- [3] B. Pan, P. Zhou, P. Lyu, H. Xiao, X. Yang, and L. Sun, *Phys. Rev. Lett.* **133**, 166701 (2024).
- [4] H.-Y. Ma, M. Hu, N. Li, J. Liu, W. Yao, J.-F. Jia, and J. Liu, *Nature Communications* **12**, 2846 (2021).
- [5] Z. Liu, M. Ozeki, S. Asai, S. Itoh, and T. Masuda, *Phys. Rev. Lett.* **133**, 156702 (2024).
- [6] G. Yang *et al.*, *Nature Communications* **16**, 1442 (2025).
- [7] Y. Wu, L. Deng, X. Yin, J. Tong, F. Tian, and X. Zhang, *Nano Lett.* **24**, 10534 (2024).

- [8] R.-W. Zhang, C. Cui, R. Li, J. Duan, L. Li, Z.-M. Yu, and Y. Yao, *Phys. Rev. Lett.* **133**, 056401 (2024).
- [9] R. Bhattacharai, P. Minch, and T. D. Rhone, *Physical Review Materials* **9**, 064403 (2025).
- [10] F. Zhang *et al.*, *Nature Physics* **21**, 760 (2025).
- [11] R. Xu, Y. Gao, and J. Liu, *National Science Review* **13**, nwaf528 (2026).
- [12] Y. Liu, J. Yu, and C.-C. Liu, *Phys. Rev. Lett.* **133**, 206702 (2024).
- [13] K. Samanta, D.-F. Shao, and E. Y. Tsymbal, *Nano Lett.* **25**, 3150 (2025).
- [14] J. Wang, X. Yang, Z. Yang, J. Lu, P. Ho, W. Wang, Y. S. Ang, Z. Cheng, and S. Fang, *Adv. Funct. Mater.* **n/a**, 2505145 (2025).
- [15] X. Zhou, W. Feng, R.-W. Zhang, L. Šmejkal, J. Sinova, Y. Mokrousov, and Y. Yao, *Phys. Rev. Lett.* **132**, 056701 (2024).
- [16] M. Gu, Y. Liu, H. Zhu, K. Yananose, X. Chen, Y. Hu, A. Stroppa, and Q. Liu, *Phys. Rev. Lett.* **134**, 106802 (2025).
- [17] Y.-Q. Li, Y.-K. Zhang, X.-L. Lu, Y.-P. Shao, Z.-Q. Bao, J.-D. Zheng, W.-Y. Tong, and C.-G. Duan, *Nano Lett.* **25**, 6032 (2025).
- [18] X. Duan, J. Zhang, Z. Zhu, Y. Liu, Z. Zhang, I. Žutić, and T. Zhou, *Phys. Rev. Lett.* **134**, 106801 (2025).
- [19] Q. Wu and L. K. Ang, *Appl. Phys. Lett.* **120**, 022401 (2022).
- [20] F. Li, B. Yang, Y. Zhu, X. Han, and Y. Yan, *Appl. Phys. Lett.* **117**, 022412 (2020).
- [21] E. Balcı, Ü. Ö. Akkuş, and S. Berber, *ACS Applied Materials & Interfaces* **11**, 3609 (2019).
- [22] X. Zhang, P. Gong, F. Liu, J. Wu, and S. Zhu, *ACS Applied Nano Materials* **5**, 15183 (2022).
- [23] H. Yu, M. Chen, Z. Shao, Y. Tao, X. Jiang, Y. Dong, J. Zhang, X. Yang, and Y. Liu, *Phys. Chem. Chem. Phys.* **25**, 10991 (2023).
- [24] Q. Chen, X. Zheng, P. Jiang, Y.-H. Zhou, L. Zhang, and Z. Zeng, *Physical Review B* **106**, 245423 (2022).
- [25] Q. Lu, W.-J. Gong, S. Li, X.-T. Zu, and H.-F. Lü, *Physical Review Applied* **22**, 024002 (2024).
- [26] Q.-Q. Li, Z.-F. Duan, W.-W. Liu, R. Yang, B. Li, and K.-Q. Chen, *Nano Research* **18**, 94907188 (2025).
- [27] Y. Feng, X. Wu, J. Han, and G. Gao, *Journal of Materials Chemistry C* **6**, 4087 (2018).
- [28] D. Waldron, V. Timosheskii, Y. Hu, K. Xia, and H. Guo, *Phys. Rev. Lett.* **97**, 226802 (2006).
- [29] L. Han *et al.*, *Science Advances* **10**, eadn0479.
- [30] Z. Zhou, X. Cheng, M. Hu, R. Chu, H. Bai, L. Han, J. Liu, F. Pan, and C. Song, *Nature* **638**, 645 (2025).
- [31] J. Tian, J. Li, H. Liu, Y. Li, Z. Liu, L. Li, J. Li, G. Liu, and J. Shi, *Physical Review B* **111**, 035437 (2025).
- [32] G. Kresse and J. Furthmüller, *Computational Materials Science* **6**, 15 (1996).
- [33] P. E. Blöchl, *Physical Review B* **50**, 17953 (1994).
- [34] J. P. Perdew, K. Burke, and M. Ernzerhof, *Phys. Rev. Lett.* **77**, 3865 (1996).
- [35] S. Grimme, *J. Comput. Chem.* **27**, 1787 (2006).
- [36] J. Taylor, H. Guo, and J. Wang, *Physical Review B* **63**, 245407 (2001).
- [37] W. Jin, G. Zhang, H. Wu, L. Yang, W. Zhang, and H. Chang, *ACS Applied Materials & Interfaces* **15**, 36519 (2023).
- [38] Z.-W. Zhang, Y.-F. Lang, H.-P. Zhu, B. Li, Y.-Q. Zhao, B. Wei, and W.-X. Zhou, *Physical Review Applied* **21**, 064012 (2024).
- [39] H.-x. Liu, Y. Honda, T. Taira, K.-i. Matsuda, M. Arita, T. Uemura, and M. Yamamoto, *Appl. Phys. Lett.* **101**, 132418 (2012).